Satellite magnetic data reveal interannual waves in Earth's core

Nicolas Gillet[a,1] , Felix Gerick[b] , Dominique Jault[a] , Tobias Schwaiger[a] , Julien Aubert[c], and Mathieu Istas[a]

The Earth's magnetic field displays variations on a broad range of time scales, from years to hundreds of millions of years. The last two decades of global and continuous satellite geomagnetic field monitoring have considerably enriched the knowledge on the rapid physical processes taking place in the Earth's outer core. Identification of axisymmetric torsional Alfvén waves with subdecadal periods from observatory and satellite data has given access to an averaged intensity of the magnetic field in the Earth's core interior. A significant part of the rapid signal, however, resides in nonaxisymmetric motions. Their origin has remained elusive, as previous studies of magnetohydrodynamic waves in the Earth's core mainly focused on their possible signature on centennial time scales. Here, we identify nonaxisymmetric wavelike patterns in the equatorial region of the core surface from the observed geomagnetic variations. These wavelike features have large spatial scales, interannual periods in the vicinity of 7 y, amplitudes reaching 3 km/y, and coherent westward drift at phase speeds of about 1,500 km/y. We interpret and model these flows as the signature of Magneto–Coriolis (MC) eigenmodes. Their identification offers a way to probe the cylindrical radial component of the magnetic field inside Earth's core. It follows from our work that there is no need for a stratified layer at the top of the core to account for the rapid geomagnetic field changes.

Earth's core | geomagnetic field variations | Magneto–Coriolis mode | satellite data

1. Introduction

The propagation of waves within the Earth's core is influenced by the Earth's rapid rotation about its axis, the background magnetic field permeating the fluid core, and possibly the buoyancy stratification. The footprint of one type of wave, the torsional Alfvén waves (or simply torsional waves), has already been found both in core surface-flow models and in length-of-day time series (1). The estimation of their period T_A, about 6 y, has been important, because T_A mainly depends on the strength B of the magnetic field in the core interior: Specifically, $T_A \sim 6$ years gives $B \sim 5$ mT. This period is a crucial time scale for the physics of the core, as it separates waves mostly influenced by rotation, the inertial waves with periods $T < T_A$, from Magneto–Coriolis (MC) waves with periods typically longer than T_A (2). We can also distinguish these different waves by their energy. In the case of torsional Alfvén waves, it is evenly distributed between their kinetic and magnetic parts, while the energy of MC (respectively [resp.], inertial) waves is predominantly magnetic (resp., kinetic). Torsional waves alone do not suffice to account for the observed interannual magnetic signal (3).

Accurate and mostly continuous monitoring of the geomagnetic field from low Earth-orbiting satellites (4) (Oersted, CHAMP, CryoSat-2, and the Swarm constellation), which began in 1999, now covers several cycles with period T_A. In addition, models built from these observations can be continued to some extent in the past, thanks to high-quality ground-based records that extend back to the late 20th century. Recently, the existence of a broad spectral peak centered on a period of ≈ 7 y has been isolated in some observatory series recorded at low latitudes (figure 3 of ref. 5). This enables us to gain insight into geomagnetic field fluctuations at the core surface, on time scales close to T_A and at large length scales (typically spherical harmonic degrees $l \lesssim 8$). At shorter periods ($T \lesssim 2$ y), we struggle to separate the magnetic field originating in the core from the ionospheric and magnetospheric fields (5).

Torsional waves consist of differential rotation between "geostrophic" cylinders, coaxial with the Earth's rotation axis, permeated by a magnetic field: They do not depend on the coordinate z along this axis (s, ϕ, z the cylindrical polar coordinates). Due to their (exactly) geostrophic nature, the Coriolis term does not enter the equilibrium of forces governing these motions. Consequently, the calculation of the period of the torsional waves is independent of the Earth's rotation rate Ω. For more general nonaxisymmetric flows (the class to which MC waves belong), the dynamics within the core at periods close to T_A is still strongly anisotropic, i.e., almost invariant in the direction parallel to the rotation axis, or quasi-geostrophic (QG) (6). The Coriolis force re-enters the momentum

Significance

The physics responsible for most of the interannual geomagnetic field changes, continually recorded by satellites for 20 years, is a long-standing open issue. By analyzing magnetic data, we detect Magneto–Coriolis waves in the Earth's outer core that account for a significant part of this signal. We further propose theoretical advances in the physical characterization of these waves, enabling a deeper understanding of the dynamics behind the geomagnetic signal. It should allow one to better sketch the heterogeneous magnetic field deep within the core, shedding further light on the mechanisms that sustain the geodynamo. Our interpretation does not require the presence of a stratified layer at the top of the core, with potent consequences regarding the Earth's thermal history.

balance because the no-penetration condition at the core–mantle boundary needs to be satisfied. For MC waves to reach periods close to T_A, the contribution of the Coriolis force to the momentum balance must be minimal, and, thus, interannual MC waves can only exhibit relatively short length scales in the cylindrical radial direction. For this reason, their magnetic footprint at the core surface was expected to be invisible in geomagnetic field models, which are limited to large length scales. This is not true close to the equator, where short length scales in the cylindrical radial direction project at the spherical core surface onto latitudinal length scales large enough to be observed in the second time derivative of the field with spherical harmonic degrees $l \lesssim 8$ (3, 7).

QG models that are valid in full spheres, including the equatorial region, where the rotation vector is parallel to the boundary, have recently been developed (8, 9). They can be combined with a description of the magnetic field that satisfies the appropriate boundary condition for a metallic core surrounded by an insulating exterior (10). We are thus now able to reproduce the observed changes of the magnetic field at the core surface with periods close to T_A. We can also construct maps of the core surface velocity from these observations and compare them with the output of QG models for the core interior. This is the approach we follow here.

2. Results

A. Core Surface Dynamics as Inferred from Magnetic Observations. We have inverted core surface flow motions for 1999–2021 (Section 4) from models of the geomagnetic field constructed using ground-based and satellite data (11, 12). The calculated flows, obtained under the spatiotemporal constraints of a geodynamo simulation, are mostly compatible with the QG hypothesis (*SI Appendix*, Fig. S1) and can thus, for a large part, be continued into the core interior. QG flows with relatively large latitudinal length scales ℓ_λ at the core surface project onto flows, with small length scales ℓ_s in the cylindrical radial direction near the equator. Then, the shear in the equatorial plane is the largest in the cylindrical radial direction. Mass conservation implies $u_s \sim u_\phi \ell_s / \ell_\phi$, with ℓ_ϕ the azimuthal length scale, so that the azimuthal flow component u_ϕ dominates. We find recurring quasi-periodic

patterns in the equatorial belt, of period $T \simeq 7$ y, propagating westward at a phase velocity $V_\phi \sim 1{,}500$ km/y or $25°/$ y (Fig. 1 *A*, *Lower*, and *SI Appendix*, Fig. S2). They are carried by low azimuthal wave numbers m, predominantly $m = 2$, and, together with torsional waves, they account for the interannual magnetic signal. Time–latitude diagrams (Fig. 1 *A*, *Upper*, and *SI Appendix*, Figs. S2 and S3) indicate outward propagation at a speed $V_s \sim 200$ km/y along the cylindrical radius s, as well as several zero-crossings in latitude. The latitude of the first one is $\lambda^\star \simeq \pm 10°$. It corresponds to a horizontal length scale at the core surface $\ell_\lambda = 2r_0\lambda^\star \sim 1{,}200$ km, where $r_0 = 3{,}485$ km is the outer core radius. Once projected onto the equatorial plane, it gives $\ell_s = r_0(1 - \cos(\lambda^\star)) \sim 50$ km.

Assuming that the mantle is electrically insulating, we focus the discussion of our results on the equatorial region. At the core surface, magnetic fluctuations **b** have to match a potential field so that $\vec{b} = -\boldsymbol{\nabla}\Phi$, where Φ is the magnetic potential. We have $|b_r| \sim (l+1)|\Phi|/r_0$ and $|b_\phi| \sim m|\Phi|/r_0$, leading to $|b_r| \sim (l+1)|b_\phi|/m$. Therefore, the two components have similar amplitude at $r = r_0$. Conversely, in the interior, the azimuthal component is much stronger than the radial component because $\ell_s \ll \ell_\phi$. For a solenoidal field, we have near the equator $|b_r| \simeq |b_s| \sim |b_\phi|\ell_s/\ell_\phi \ll |b_\phi|$. The relative magnitude of the magnetic and kinetic parts can be estimated in the interior from the linearized induction equation

$$\frac{\partial \mathbf{b}}{\partial t} = \boldsymbol{\nabla} \times (\mathbf{u} \times \mathbf{B}_0) + \eta \nabla^2 \mathbf{b}, \qquad [1]$$

with η the magnetic diffusivity and $\mathbf{B}_0$ the slowly evolving background field. Assuming diffusion does not affect much the rapid changes in the magnetic field, as it is the case in Earth-like geodynamo simulations (13), the magnetic field perturbation in the interior scales as $|b_\phi| \sim |B_{0,r}||u_\phi|/\omega\ell_s$, with $\omega = 2\pi/T$. We can transform this result into a magnetic to kinetic energy ratio in the interior

$$\frac{1}{\rho\mu}\frac{|\mathbf{b}|^2}{|\mathbf{u}|^2} \sim \frac{|B_{0,r}|^2}{\rho\mu(\omega\ell_s)^2} \approx 10 \qquad [2]$$

with $\rho \simeq 10^4$ kg/m^3 the core density, $\mu = 4\pi \times 10^{-7}$ H/m its magnetic permeability, and $|B_{0,r}| = 5 \times 10^{-4}$ T an estimate of the radial magnetic field at the core surface in the equatorial region
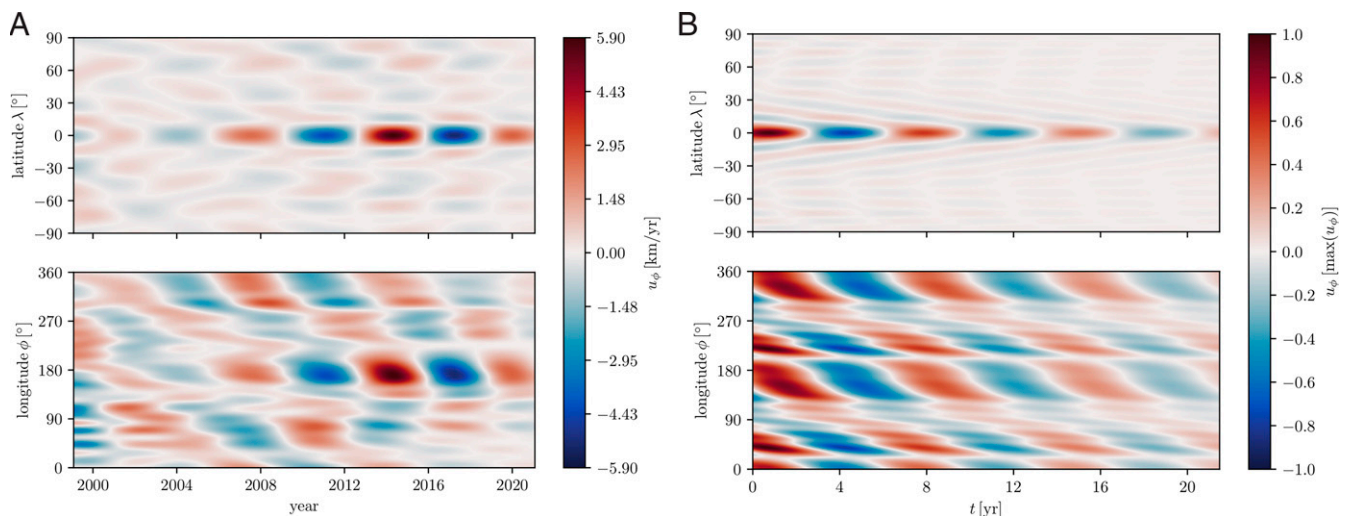
Fig. 1. Propagation of interannual flow patterns at the core surface. (*A*) Surface azimuthal velocity inverted from the CHAOS-7 geomagnetic field model, bandpass-filtered between 4 and 9.5 y (Section 4), as a time–longitude diagram at the equator (*Lower*) and a time–latitude diagram at the longitude $\phi = 170°$ (*Upper*). (*B*) Same representation for one example of a calculated QG MC mode of period 7.16 y and azimuthal wave number mainly $m = 2$, with the time–latitude diagram shown at the longitude $\phi = 219°$ (Section 4).

(14). This result agrees with the classification of the waves we have detected as MC waves, whose energy is mostly magnetic. From Eq. **1** below the equator, we get $|b_r| \sim m|B_{0,r}||u_\phi|/(\pi r_0 \omega)$, with m the azimuthal wave number of the magnetic perturbation. As a result, using the continuity of b_r and of u_ϕ across the boundary layer, the magnetic to kinetic energy ratio at the core–mantle boundary behaves as

$$\frac{1}{\rho\mu}\frac{|\mathbf{b}|^2}{|\mathbf{u}|^2} \sim \frac{m^2|B_{0,r}|^2}{\rho\mu(\omega\pi r_0)^2} \approx 2m^2 \times 10^{-4}. \qquad \textbf{[3]}$$

It is $\lesssim 10^{-2}$ for observable length scales. Using $|u_\phi| \sim 4$ km/y (Fig. 1), we find $b_r \sim 1$ μT for $m = 5$, in agreement with interannual field changes observed at the core surface (3, 7). The difference between the kinetic to magnetic energy ratio at the surface and in the interior is one reason why a detection of such waves is difficult from the magnetic field alone, as has been the case for torsional waves (1). Eq. **3** tends to indicate that the direct extraction of waves from magnetic field models is easier for their high m part. As a matter of fact, previous investigations of equatorial waves emphasized magnetic structures with wave number $m = 5 - 6$ (3), whereas the present study, relying on core surface flows, focuses on $m = 2$ components.

Field changes induced by the recovered flow at interannual periods account well for the oscillations in the rate of change of the magnetic field observed above the Earth's surface, in particular near the equator. This is well illustrated by low latitudes observatory series (Fig. 2). Still, subgrid processes play a significant role (*SI Appendix*, Figs. S4 and S5). Maps of the interannual induction at the core surface show a clear correlation between these two sources of magnetic field changes (*SI Appendix*, Fig. S6). This is a property shared with geodynamo simulations (*SI Appendix*, Fig. S7).

B. QG MC eigenmodes. We have computed linear solutions to the QG model in the presence of a nonaxisymmetric poloidal background field $\mathbf{B}_0$, accounting for weak magnetic diffusion

as in the Earth (Section 4). The computed eigenmodes include QG inertial (or Rossby) modes at periods shorter than T_A, torsional Alfvén modes at periods around T_A, and QG MC modes with periods longer than T_A. In Fig. 1*B*, we show time–latitude (*Upper*) and time–longitude (*Lower*) diagrams for the surface azimuthal velocity of a QG MC mode with a period $T \simeq 7.16$ y and a much longer decay time of 92.56 y. It is readily seen that the numerical QG MC mode compares well with the flow inferred from observations (Fig. 1). The mode is characterized by small length scales in the latitudinal direction and larger length scales in longitude. The complexity observed in the time–longitude diagram for the flow reflects the mixing of azimuthal orders m, in link with azimuthal variations in $\mathbf{B}_0$ (see *SI Appendix*, Fig. S10 and the local dispersion relation below). Because $\mathbf{B}_0$ is nonaxisymmetric, eigensolutions mix azimuthal orders m. Still, motions for interannual eigenmodes are dominated by low m patterns. For our particular choice of background field, it happens that eigenmodes separate between modes whose flow presents only even or odd orders m (Section 4). Among the whole set of calculated MC eigenmodes, the one presented here is dominated by a $m = 2$ flow structure and presents nine zero crossings in the radial direction. The azimuthal complexity of the magnetic perturbation is higher (Fig. 3), as a result of the magnetic boundary condition (Section 2A).

The mode features propagation toward the equator, similar to the flow recovered from observations. The velocity peaks near the equator, with the first zero crossing at $\lambda^\star \simeq \pm 10°$. The time–longitude diagram shows a clear westward propagation of the mode. Notwithstanding their small cylindrical radial length scale, QG flows project on surface flows with large length scales in the latitudinal direction in the equatorial region of the core surface. This is also seen in Fig. 3 *A* and *B*, which illustrate, respectively, the surface flow and magnetic field perturbations of the mode for a snapshot in time. In order to compare the magnetic and the kinetic energies, we transform the magnetic field into a quantity that has the dimension of a velocity: $\mathbf{b}/\sqrt{\rho\mu}$. Its radial component $b_r/\sqrt{\rho\mu}$ at the core surface is a factor six times smaller than the
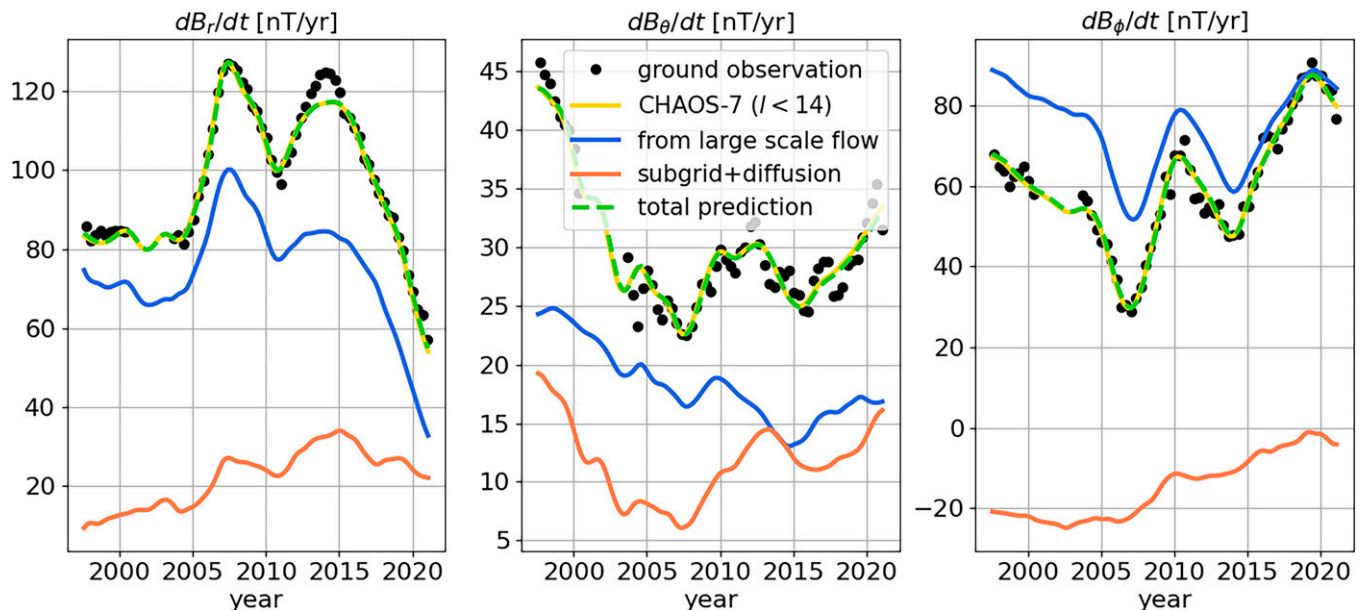
Fig. 2. Contributions to the rate of change of the magnetic field at an observatory near the equator. Observations (15) (black dots; in nT/y) cleaned for the contributions from external signals (16) for the three components measured at the Ascension Island observatory (8°S, 27°W), superimposed with predictions from the CHAOS-7 model truncated at degree $l = 13$ (yellow) and the contributions from the ensemble average of the large-scale flow (blue) and of the errors of representativeness resulting primarily from subgrid processes (orange; Section 4), inverted from the CHAOS-7 Gauss coefficient data. The total contribution (dashed green) almost superimposes with the CHAOS-7 data. The recorded interannual oscillations, in particular toward low latitudes, are clearly associated with some fluctuations in the large length-scale flow.
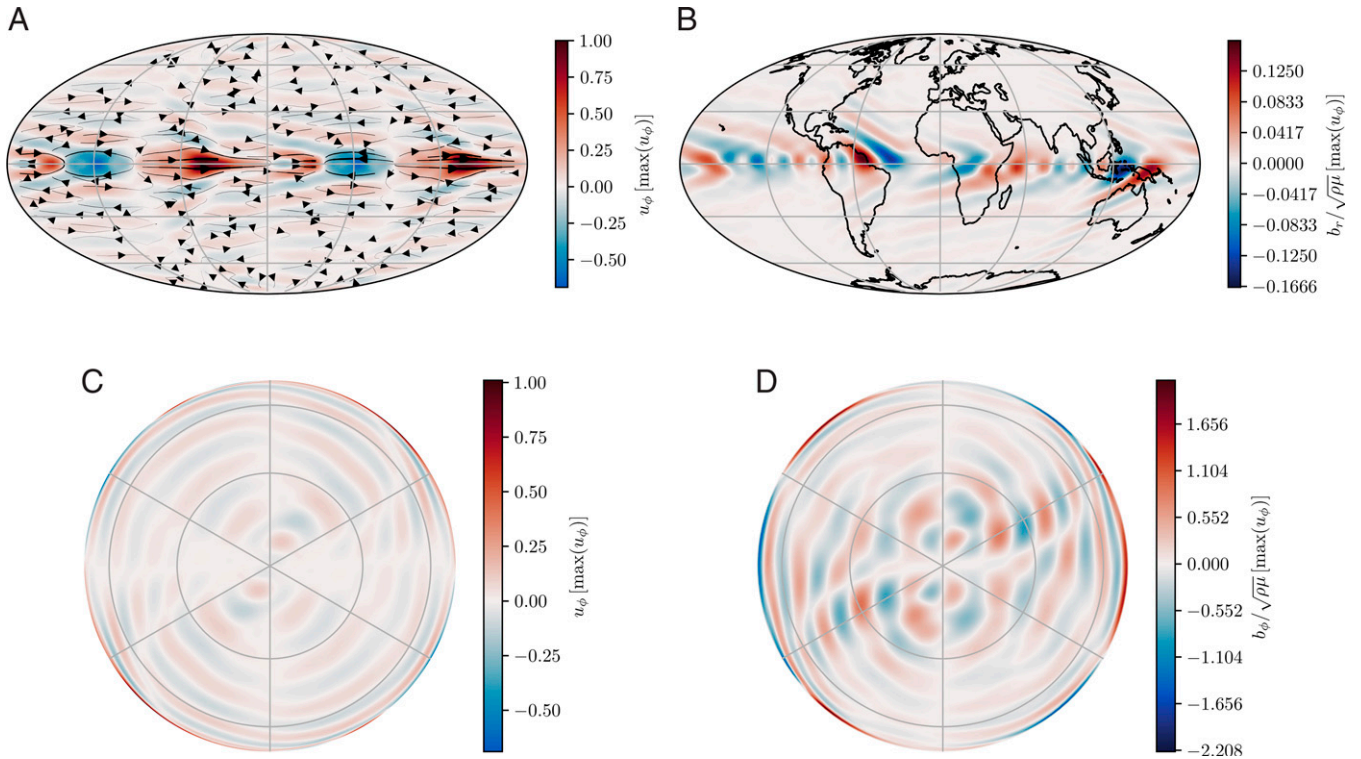
Fig. 3. QG MC eigenmode of period $T = 7.16$ y. Its flow component, of even order m (Section 4), is dominated by an azimuthal wave number $m = 2$. Mollweide projection of the flow (A) and the radial magnetic field $b_r/\sqrt{\rho\mu}$ (B) at the core surface. Equatorial cross-section of the azimuthal flow u_ϕ (C) and magnetic field $b_\phi/\sqrt{\rho\mu}$ (D). Both **u** and $\mathbf{b}/\sqrt{\rho\mu}$ have been normalized to the maximum azimuthal velocity value. Grid lines in the equatorial slices correspond to the grid lines of the surface projections.

flow, in qualitative agreement with the observations at interannual periods. QG eigenmodes present a strong cylindrical radial shear of the z-invariant azimuthal velocity, in particular in the vicinity of the equator. This translates into a much stronger azimuthal magnetic field perturbation in the bulk of the core, as we expect from the scale analysis outlined in the previous section. Deep in the core, the magnetic field perturbation dominates the velocity (see equatorial slices in Fig. 3 *C* and *D*), with the magnetic energy $|\mathbf{b}|^2/(2\mu)$ larger than the kinetic energy $\rho|\mathbf{u}|^2/2$ by a factor of ≈ 36 (averaged over the volume). This is in agreement with Eq. **2** and the energy ratio anticipated for MC eigenmodes (10). The distinction between the strength of the perturbation at the surface and in the bulk is more easily seen in the azimuthal rms values,

$\langle f \rangle (s, z) = \sqrt{\dfrac{1}{2\pi} \oint f(s, \phi, z)^2 \, \mathrm{d}\phi}$, of the velocity and the mag-

netic field perturbation, evaluated at the core surface ($z = H = \sqrt{r_0^2 - s^2}$) and in the equatorial plane ($z = 0$), as shown in Fig. 4. In the equatorial plane, the dominant component is along the azimuth, with $\langle b_\phi \rangle (s, 0)$ dominating over $\langle b_r \rangle (s, 0)$ for $s/r_0 \gtrsim 0.5$. Except in the vicinity of the equator, where $\langle b_r \rangle (s, 0)$ and $\langle b_r \rangle (s, H)$ tend to superimpose, the magnetic perturbation is much stronger in the bulk than at the surface. Deep in the core, the velocity component of the mode is weaker than the magnetic one everywhere, with $\langle u_\phi \rangle (s)$ less than $\langle b_\phi \rangle (s, 0)/\sqrt{\rho\mu}$. Only close to the surface (and in particular the equator), the kinetic part of the mode dominates. At the core surface, the magnetic to kinetic energy ratio of the torsional Alfvén and the QG MC eigenmodes decreases with their frequency (*SI Appendix*, Figs. S8 and S9).

3. Discussion

The frequency of rapid MC waves depends on the strength $B_{0,s}$ of the magnetic field in the cylindrical radial direction when

they have large radial wave number k. With this hypothesis, and neglecting the subdominant magnetic dissipation, we can derive a local dispersion relationship (Section 4) and obtain a wave number

$$k_0 = \left(\frac{m\Omega}{V_A H^2} \right)^{1/3}, \qquad [4]$$

above which only Alfvén waves exist and below which we can separate inertial (Rossby) waves from MC waves, with
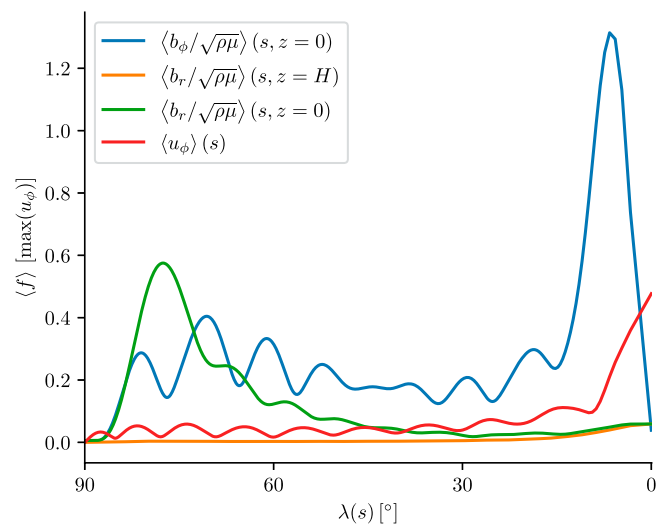
Fig. 4. Latitudinal profiles of the rms azimuthal flow $\langle u_\phi \rangle (\lambda(s))$ and magnetic field perturbations $\langle b_\phi \rangle (\lambda(s), z = 0)/\sqrt{\rho\mu}$ and $\langle b_r \rangle (\lambda(s), z = 0)/\sqrt{\rho\mu}$ in the equatorial plane and $\langle b_r \rangle (\lambda(s), z = \pm H)/\sqrt{\rho\mu}$ at the core surface. All profiles have been normalized to the maximum velocity value. The latitude $\lambda(s) = \arctan(H(s)/s)$ is that of the circle on the spherical surface intersecting the geostrophic cylinder of radius s. The profiles correspond to the eigenmode shown in Fig. 3.

$$V_A(s,\phi) = \sqrt{\frac{1}{2H} \int_{-H}^{H} \frac{1}{\rho\mu} B_{0,s}^2(s,\phi,z)\,dz}, \qquad \textbf{[5]}$$

the local Alfvén velocity. Here, we have used the plane wave ansatz $\mathbf{u}(s,\phi,t) \propto \exp\left(i(m\phi + ks - \omega t)\right)$. MC waves (for $k \leq k_0$) have frequencies

$$\omega_{MC} = -\frac{V_A^2 k^4 H^2}{2m\Omega} \qquad \textbf{[6]}$$

where the minus sign means westward propagation. It is because of their very dispersive nature that QG MC waves can reach interannual periods. They have a frequency similar to that of torsional waves when k is not much smaller than k_0. Translated to the core conditions, it gives $k_0 r_0 \gtrsim 30$ for $B_{0,s} \approx 3$ mT and $H = r_0/2$, in agreement with the radial complexity of the eigenmodes that we have calculated (Fig. 3 ; $kr_0/2\pi = 5$). QG MC waves may propagate along either the radial or azimuthal directions or present spiraling patterns at the core surface, depending on their wave numbers and on the background field. Their phase speed inferred from patterns in time–latitude and time–longitude diagrams at the core surface will thus enable us to constrain the quantity $V_A^2(s,\phi)$. In comparison, torsional waves only give information on the ϕ integral of $V_A^2(s,\phi)$ (17). Therefore, the study of MC waves complements the investigation of torsional waves and will make it possible to gain knowledge on the geometry of the magnetic field in the core interior. The dispersion relation [**6**], similarly to that of torsional waves, does not depend on the azimuthal component of the magnetic field. In this respect, our work differs from previous analyses of MC waves, which dealt with centennial or longer time scales (18). In fact, most previous studies used toroidal zonal fields as background magnetic fields (19), whereas we find that it is not this part of the background field that mostly supports rapid MC waves. Finally, the magnetic perturbations at the core surface are predominantly equatorially symmetric at low latitudes (*SI Appendix*, Fig. S6). Our investigations reveal that the symmetry of MC eigenmodes relates to that of the background field.

The observed interannual field changes had recently been explained in terms of Alfvén waves with small radial length scales, from a series of numerical geodynamo simulations (6, 13). We favor an alternative interpretation, where the Coriolis acceleration enters the momentum balance. At the length and time scales that are accessible today, the importance of the Coriolis force is inevitable near the equator. It implies that the detection of Alfvén waves, associated with the dispersion relation [**21**], would require an improved spatiotemporal resolution.

Waves carry information on the properties of the medium they pass through. The physical framework that we propose here to understand rapid changes in the core surface flow thus offers a way to map the field $\mathbf{B}_{0,s}$ deep in the core, where it cannot be probed only based on the information brought by observations. The apparent outward propagation (in opposition to standing oscillation) of wave patterns may be related to magnetic dissipation in the bulk, as for our calculated eigenmodes. Alternatively, it may also be related to core–mantle coupling, as in the case of torsional waves (14, 20), or to a superposition of two modes. The latter scenario cannot be excluded, given the limited frequency resolution available with only two decades of satellite records. The description in terms of QG MC dynamics allows us to understand the relative temporal spectra, $S_B(\omega)$ and $S_U(\omega)$, for, respectively, the magnetic field and the flow. The former is much steeper than the latter and evolves as $S_B \propto \omega^{-4}$ for periods from about T_A to several decades (21). This observation is compatible with a

magnetic to kinetic energy ratio $\propto S_B/S_U$ that increases toward low frequencies (8, 10). Combined with a magnetic energy mostly confined below the core surface, this renders the detection of QG MC waves from the flow easier than from the magnetic field. This observation calls for further investigations of core surface flow reconstructions at longer (decadal) periods (22), as inferred from ground-based and satellite magnetic records.

Finally, we propose a parsimonious interpretation of magnetic data, where the only required ingredients are the presence of global rotation and a magnetic field presenting a cylindrical radial component. Magnetic dissipation plays a secondary role here. It transpires that only a few modes are needed to explain the observed wavelike evolution of the velocity and magnetic fields. Our scenario constitutes an alternative to an explanation based on waves trapped into a stratified layer at the top of the core (23). As waves carried by a combination of magnetic, Coriolis, and buoyancy forces can involve short radial length scales, their dynamics is potentially compatible with the interannual time scale of the observed magnetic acceleration (24). The presence of a stratified layer was motivated by evidences from seismology or mineral physics (25, 26), which are currently debated (27, 28). Any information on a stratified layer at the top of the core would be crucial when building models for the evolution of the Earth (29, 30). Our analysis of interannual magnetic changes from satellite records requires no such layer.

4. Methods

A. Geomagnetic Field Models. We use as observations Gauss coefficients from geomagnetic field models. We consider both CHAOS-7 (11) (1999–2021) and COV-OBS-x2 (12) (1840–2020). These are built from ground-based and satellite data, the latter being included in COV-OBS-x2 by means of geomagnetic virtual observatories (31). Both models are projected in time on splines: of order 4 with knots spacing 2 y for COV-OBS-x2 and of order 6 with knot spacing 6 mo for CHAOS-7. Another important difference between the two models is associated with the prior information used to reduce nonuniqueness. CHAOS-7 is a regularized field model that penalizes the third time derivative plus the second time derivative near the endpoints, while in COV-OBS-x2, a stochastic prior coherent with the occurrence of geomagnetic jerks is imposed using temporal cross-covariances. Also note that near zonal coefficients are more heavily damped in CHAOS-7, in order to reduce the leakage of unmodeled signals at high latitudes.

B. Reconstruction of Core Surface Flow Motions. The flow models have been inverted with the pygeodyn data-assimilation algorithm (32). This tool uses an augmented state-ensemble Kalman filter that forecasts a stochastic model of the core surface dynamics (22). The latter is anchored to spatiotemporal statistics derived from the 71%-path geodynamo simulation (13). The core surface flow is inverted from the radial component of the induction equation at the core surface,

$$\frac{\partial \overline{B}_r}{\partial t} = -\overline{\nabla_H \cdot \left(\mathbf{u}\overline{B}_r\right)} + e_r, \qquad \textbf{[7]}$$

where overlines stand for the projection onto spherical harmonic degrees $l \leq L_b = 13$. The flow is truncated at degree $L_u = 18$. The last term e_r in Eq. **7** stands for errors of representativeness, which incorporate all contributions to the rate of change of the field that involve small length-scale fields (degrees $l > L_u$ and $l > L_b$ for, respectively, the flow and the magnetic field), plus diffusion. The separate contributions from e_r and $\mathbf{u}$ to geomagnetic field changes are illustrated in *SI Appendix*, Fig. S5 with some examples of Gauss coefficients and in Fig. 2 and *SI Appendix*, Fig. S4 with predictions to several ground-based observatories.

A first inversion has been performed using as observations Gauss coefficients that describe the rate of change of magnetic field (or secular variation) from the COV-OBS-x2 model over 1880–2020. This initial flow model has been used as the starting state for the inversion of a second model over 1999–2021 from the CHAOS-7 field model. The obtained solutions thus extend previous models (22) to more recent epochs. In both cases, secular variation data uncertainties

are estimated from the spread within the ensemble of COV-OBS-x2 models and depend on time. Ensembles of 50 realizations have been calculated. The two decades covered by satellite data limit the period range where flow models are best resolved to time scales shorter than 10 y. Within this subdecadal range, a spectral line at $T \approx 7$ y has been isolated in ground-based series recorded in the vicinity of the equator (5). To focus on the source of this interannual signal, we band-pass filter the obtained flow models for periods between 4 and 9.5 y, with an order 4 causal Butterworth filter.

C. Computation of the QG MC Eigenmodes. The flow perturbation $\mathbf{u}$ over a mean state $[\mathbf{u}_0 = \mathbf{0}, \mathbf{B}_0]$ of an inviscid and electrically conducting planetary core under rapid rotation can be described by the linearized momentum equation

$$\frac{\partial \mathbf{u}}{\partial t} = -2\Omega \mathbf{1}_z \times \mathbf{u} - \frac{1}{\rho} \boldsymbol{\nabla} p$$
$$+ \frac{1}{\mu\rho} \left((\boldsymbol{\nabla} \times \mathbf{B}_0) \times \mathbf{b} + (\boldsymbol{\nabla} \times \mathbf{b}) \times \mathbf{B}_0 \right), \quad [8]$$

complemented by the induction Eq. **1**. To compute eigenmodes of this system for nonidealized mean fields and sufficient spatial complexity, we consider further simplifications. We exploit the columnarity of magnetohydrodynamic flows under rapid rotation (33). Then, the flow can be described as QG, so that

$$\mathbf{u} = \boldsymbol{\nabla} \psi \times \boldsymbol{\nabla} \left(\frac{z}{H} \right), \quad [9]$$

with $\psi = \psi(s, \phi, t)$ the stream function and $H = \sqrt{r_0^2 - s^2}$ the half height of the fluid column. By projecting the three-dimensional (3D) momentum Eq. **8** onto the subset of QG velocities [**9**], a reduced model for a fully liquid core is obtained, where the velocity is described by the evolution of ψ in the equatorial plane (8). This reduced momentum equation is combined with a 3D magnetic field that matches a potential field at the core–mantle boundary, i.e., the mantle is assumed to be insulating (10). We choose orthonormal velocity and magnetic field bases for the projection to obtain a standard, instead of a generalized, eigen problem, substantially improving convergence of the eigen solver. For the velocity basis, we use the orthogonal QG inertial eigenmodes, which can be written explicitly (34). The magnetic field basis presented in Gerick et al. (10) is orthonormalized by using a modified Gram–Schmidt method.

We impose a poloidal background magnetic field $\mathbf{B}_0$ designed so that it satisfies geophysical constraints associated with the phase velocity $\sqrt{\langle V_A^2(s, \phi) \rangle}$ of (geostrophic) torsional eigenmodes (1, 14):

$$\max \left(\sqrt{\rho\mu \langle V_A^2 \rangle} \right) \simeq 3 \, \text{mT} \quad [10a]$$

$$\sqrt{\rho\mu \langle V_A^2 \rangle}\big|_{s=1} \simeq 0.45 \, \text{mT}. \quad [10b]$$

The background field is defined as

$$\mathbf{B}_0 = \sum_{m=-1}^{0} \sum_{n=0}^{1} \beta_{l=1,m,n} \hat{\mathbf{B}}_P(l=1, m, n), \quad [11]$$

where $\hat{\mathbf{B}}_P(l, m, n)$ are the basis vectors given by equation A21 in Gerick et al. (10), normalized to have unit energy. Here, l and m correspond to the spherical harmonic degree and order, respectively, and n is the radial degree. The coefficients $\beta_{l,m,n}$ are given by $\beta_{1,0,0} \approx -2.3$, $\beta_{1,0,1} \approx 1.45$, $\beta_{1,-1,0} \approx 2.04$, and $\beta_{1,-1,1} \approx -1.77$, so that $\left(\int \mathbf{B}_0^2 \, dV \right)^{1/2} \approx 12.7 \, \text{mT}$. The choice for the coefficients $\beta_{l,m,n}$, based on the requirements in Eq. **10**, results in a period for the gravest torsional Alfvén mode about 6 y (1). A nonaxisymmetric $\mathbf{B}_0$ with $m = -1$ is chosen, so that $\langle V_A^2 \rangle(s) \neq 0$ everywhere, in particular at $s = 0$. This requirement is crucial for the existence of diffusionless torsional Alfvén modes (35). It seems to be relevant as well for obtaining numerically converged MC eigenmodes in the interannual period range, with or without diffusion (although $\eta \neq 0$ slightly helps for numerical convergence). The background field in Eq. **11** includes the two largest Gauss coefficients in the Earth's magnetic field exterior

to the core [here, the time-averaged CHAOS-7 model (11)], with the correct ratio of their amplitude, but nine times larger so that requirement Eq. **10b** is met.

Our background field presents point antisymmetry with respect to $\mathbf{r} = \mathbf{0}$: $\mathbf{B}_0(\mathbf{r}) = -\mathbf{B}_0(-\mathbf{r})$. As a consequence, the QG modes separate between modes for which the flow is either symmetrical or antisymmetrical with respect to $\mathbf{r} = \mathbf{0}$ (and vice versa for the magnetic part of the mode). QG flows are furthermore symmetrical with respect to the equatorial plane [$\mathbf{u}_e(z) = \mathbf{u}_e(-z)$, $u_z(z) = -u_z(z)$, where $\mathbf{u}_e$ denotes the equatorial flow component]. As a result, $\mathbf{u}_e$ is either symmetrical with respect to a rotation of angle π about the axis ($\mathbf{u}_e(s, \phi) = \mathbf{u}_e(s, \phi + \pi)$) or antisymmetrical ($\mathbf{u}_e(s, \phi) = -\mathbf{u}_e(s, \phi + \pi)$). In the first (resp., second) instance, the mode presents only odd (resp., even) m. The same reasoning does not hold for the magnetic part of the mode because it is not equatorially symmetrical. The flow for the selected eigenmode of period 7.16 y has only even m.

Higher orders of the background magnetic field are not included here, to ensure numerical convergence of the eigensolutions. The latter is verified by requiring a decay in the kinetic and magnetic energy of the eigenmodes as a function of polynomial degree, shown in *SI Appendix*, Fig. S11 for the modes discussed above. In *SI Appendix*, Fig. S10, we show profiles of $\sqrt{\rho\mu}V_A(s, \phi)$ at several longitudes and a map of $B_{0,r}(\theta, \phi)$ at the core surface. Defining $B_0 = \left(\int \mathbf{B}_0^2 \, dV \right)^{1/2}$, the Lehnert number associated to this background magnetic field is $\text{Le} = B_0/(\Omega r_0 \sqrt{\mu_0 \rho}) \approx 4.3 \times 10^{-4}$. We choose $\eta \approx 3.76 \, \text{m}^2/\text{s}$, within the range of acceptable geophysical values (27, 36), so that the Lundquist number (the number of Alfvén times per magnetic diffusion time r_0^2/η) is $\text{Lu} = B_0 r_0/(\eta\sqrt{\mu_0 \rho}) \simeq 10^5$. As a consequence, the calculated eigenmodes are only secondarily affected by magnetic damping, with decay times much longer than their period.

We focus on several eigenmodes near the target period of 7 y using the shift-invert Arnoldi method. Many other modes at longer and shorter periods exist, but are not of interest in the context discussed here. The calculated QG MC eigenmodes with interannual periods show quality factors (i.e., the ratio of their frequency to their decay rate) larger than 10 and therefore propagate before being damped by Ohmic dissipation.

D. Reduced Dispersion Relation of Interannual QG-MC Waves. We write the streamfunction as $\psi(s, \phi) = H^3 \psi_1(s, \phi)$, where ψ_1 is regular at $s = 1$ in order to ensure regularity of $\mathbf{u}$ at the equator, where $H = 0$. We assume that radial length scales are much shorter than horizontal length scales, or $kr_0 \gg m/(2\pi)$. In order to derive the evolution equation for ψ, we project the momentum equation onto trial functions (8):

$$-2\frac{\partial}{\partial t}\mathcal{L}^2(\psi) - \frac{4\Omega}{sH^2}\frac{dH}{ds}\frac{\partial\psi}{\partial\phi} = \frac{1}{\rho\mu s}\frac{\partial}{\partial s}\left(\frac{1}{sH}\frac{\partial}{\partial s}\left(s^2 \{B_s B_\phi\} \right) \right). \quad [12]$$

Here, we have kept only the highest derivatives in s in the expression of the magnetic force, in a configuration where the azimuthal field is not significantly larger than the radial one, as suggested by geodynamo simulations outside of the geostrophic cylinder attached to the inner core (37). The curly brackets {} denote the z-integral (38),

$$\{B_s B_\phi\} = \int_{-H}^{H} B_s B_\phi \, dz, \quad [13]$$

and the operator $\mathcal{L}^2$ is defined as

$$\mathcal{L}^2(\psi) = \boldsymbol{\nabla} \cdot \left(\frac{1}{H}\boldsymbol{\nabla}\psi \right) + \frac{1}{3s^2 H}\left(\frac{dH}{ds} \right)^2 \frac{\partial^2\psi}{\partial\phi^2}. \quad [14]$$

For a spherical core $dH/ds = -s/H$, so that the momentum Eq. **12**, expressed for ψ_1, becomes

$$H^3 \frac{\partial}{\partial t}\left(\mathcal{L}^2(\psi_1) \right) - 2\Omega \frac{\partial\psi_1}{\partial\phi} = -\frac{1}{2\rho\mu H}\frac{\partial^2}{\partial s^2}\{B_s B_\phi\}, \quad [15]$$

under the condition $kH \ll |dH/ds|$. The time evolution of the quantity $\{B_s B_\phi\}$ is given by the linearized induction equation, where we keep, again, only the highest derivative in s:

$$\frac{\partial}{\partial t}\{B_s B_\phi\} = -H^2 \{B_{0,s}^2\} \frac{\partial^2 \psi_1}{\partial s^2}. \qquad \textbf{[16]}$$

Here, we have neglected magnetic dissipation, as it plays a secondary role for decadal to interannual geomagnetic field changes (13) and because the calculated eigenmodes present decay times much longer than their periods. Finally, by coupling [**15**] and [**16**], an evolution equation for ψ_1 is obtained. Assuming that the radial wavelength of the perturbation is much shorter than the length scale over which the medium (H, s, $\{B_{0,s}^2\}$) evolves, we get

$$\frac{\partial^4 \psi_1}{\partial t^2 \partial s^2} - \frac{2\Omega}{H^2}\frac{\partial^2 \psi_1}{\partial t \partial \phi} = V_A^2 \frac{\partial^4 \psi_1}{\partial s^4}, \qquad \textbf{[17]}$$

where V_A is given by Eq. **5**. Under the plane-wave ansatz $\psi_1 \propto \exp(i(ks + m\phi - \omega t))$, it gives

$$\omega^2 - \frac{2\Omega m}{(kH)^2}\omega - V_A^2 k^2 = 0, \qquad \textbf{[18]}$$

leading to the dispersion relation

$$\omega = \frac{m\Omega}{k^2 H^2} \pm \sqrt{\left(\frac{m\Omega}{k^2 H^2}\right)^2 + V_A^2 k^2}. \qquad \textbf{[19]}$$

This latter can also be written as

$$\omega = V_A k \left((k_0/k)^3 \pm \sqrt{1 + (k_0/k)^6}\right), \qquad \textbf{[20]}$$

with k_0 given by Eq. **4**. In the small wavelength limit ($k \gg k_0$), we have at the first order in $(k_0/k)^3$

$$\omega \simeq V_A k \left(\pm 1 + (k_0/k)^3\right) = \pm V_A k + \frac{m\Omega}{k^2 H^2}. \qquad \textbf{[21]}$$

Then, the wave frequency ω only weakly departs from the Alfvén wave frequency. These waves have been found in dynamo simulations, where they have been called QG Alfvén waves (6, 13).

In the opposite limit $k \ll k_0$, from [**19**], Rossby waves and MC waves are clearly separated, with frequencies, respectively,

$$\omega_R = \frac{2m\Omega}{(kH)^2} \text{ and } \omega_{MC} = -\frac{V_A^2 H^2 k^4}{2\Omega m} = -\frac{\Omega \text{Le}^2 (kH)^4}{2m}, \qquad \textbf{[22]}$$

where $\text{Le} = V_A/(H\Omega)$ compares the rotation frequency and the Alfvén wave frequency. The period of MC waves is distinct from that of Rossby or QG Alfvén waves only for large length scales ($k \le k_0$). They have frequencies similar to the torsional waves frequency kV_A if their wave number k does not differ too much from k_0.

1. N. Gillet, D. Jault, E. Canet, A. Fournier, Fast torsional waves and strong magnetic field within the Earth's core. *Nature* **465**, 74–77 (2010).
2. R. Hide, Free hydromagnetic oscillations of the Earth's core and the theory of the geomagnetic secular variation. *Philos. Trans. R. Soc. Lond. A* **259**, 615–647 (1966).
3. A. Chulliat, S. Maus, Geomagnetic secular acceleration, jerks, and a localized standing wave at the core surface from 2000 to 2010. *J. Geophys. Res. Solid Earth* **119**, 1531–1543 (2014).
4. M. D. Hammer, C. C. Finlay, N. Olsen, Applications for CryoSat-2 satellite magnetic data in studies of Earth's core field variations. *Earth Planets Space* **73**, 1–22 (2021).
5. V. Lesur, N. Gillet, M. D. Hammer, M. Mandea, Rapid variations of Earth's core magnetic field. *Surv. Geophys.*, 10.1007/s10712-021-09662-4 (2022).
6. J. Aubert, C. C. Finlay, Geomagnetic jerks and rapid hydromagnetic waves focusing at Earth's core surface. *Nat. Geosci.* **12**, 393–398 (2019).
7. C. C. Finlay, N. Olsen, S. Kotsiaros, N. Gillet, L. Tøffner-Clausen, Recent geomagnetic secular variation from Swarm and ground observatories as estimated in the CHAOS-6 geomagnetic field model. *Earth Planets Space* **68**, 112 (2016).
8. F. Labbé, D. Jault, N. Gillet, On magnetostrophic inertia-less waves in quasi-geostrophic models of planetary cores. *Geophys. Astrophys. Fluid Dyn.* **109**, 587–610 (2015).
9. O. P. Bardsley, Could hydrodynamic Rossby waves explain the westward drift? *Proc. Math. Phys. Eng. Sci.* **474**, 20180119 (2018).
10. F. Gerick, D. Jault, J. Noir, Fast quasi-geostrophic Magneto-Coriolis modes in the Earth's core. *Geophys. Res. Lett.* **48**, e2020GL090803 (2021).
11. C. C. Finlay et al., The CHAOS-7 geomagnetic field model and observed changes in the South Atlantic Anomaly. *Earth Planets Space* **72**, 156 (2020).
12. L. Huder, N. Gillet, C. C. Finlay, M. D. Hammer, H. Tchoungui, COV-OBS.x2: 180 years of geomagnetic field evolution from ground-based and satellite observations. *Earth Planets Space* **72**, 160 (2020).
13. J. Aubert, N. Gillet, The interplay of fast waves and slow convection in geodynamo simulations nearing Earth's core conditions. *Geophys. J. Int.* **225**, 1854–1873 (2021).
14. N. Gillet, D. Jault, E. Canet, Excitation of travelling torsional normal modes in an Earth's core model. *Geophys. J. Int.* **210**, 1503–1516 (2017).
15. S. Macmillan, N. Olsen, Observatory data and the Swarm mission. *Earth Planets Space* **65**, 1355–1362 (2013).
16. N. Olsen et al., The CHAOS-4 geomagnetic field model. *Geophys. J. Int.* **197**, 815–827 (2014).
17. S. I. Braginsky, Torsional magnetohydrodynamic vibrations in the Earth's core and variations in day length. *Geomagn. Aeron.* **10**, 1–8 (1970).
18. C. C. Finlay, A. Jackson, Equatorially dominated magnetic field change at the surface of Earth's core. *Science* **300**, 2084–2086 (2003).
19. K. Hori, R. J. Teed, C. A. Jones, The dynamics of magnetic Rossby waves in spherical dynamo simulations: A signature of strong-field dynamos? *Phys. Earth Planet. Inter.* **276**, 68–85 (2018).
20. N. Schaeffer, D. Jault, Electrical conductivity of the lowermost mantle explains absorption of core torsional waves at the equator. *Geophys. Res. Lett.* **43**, 4922–4928 (2016).
21. A. De Santis, D. Barraclough, R. Tozzi, Spatial and temporal spectra of the geomagnetic field and their scaling properties. *Phys. Earth Planet. Inter.* **135**, 125–134 (2003).
22. N. Gillet, L. Huder, J. Aubert, A reduced stochastic model of core surface dynamics based on geodynamo simulations. *Geophys. J. Int.* **219**, 522–539 (2019).
23. B. Buffett, H. Matsui, Equatorially trapped waves in Earth's core. *Geophys. J. Int.* **218**, 1210–1225 (2019).
24. A. Chulliat, P. Alken, S. Maus, Fast equatorial waves propagating at the top of the Earth's core. *Geophys. Res. Lett.* **42**, 3321–3329 (2015).
25. G. Helffrich, S. Kaneshima, Outer-core compositional stratification from observed core wave speed profiles. *Nature* **468**, 807–810 (2010).
26. K. Ohta, T. Yagi, K. Hirose, Y. Ohishi, Thermal conductivity of ferropericlase in the Earth's lower mantle. *Earth Planet. Sci. Lett.* **465**, 29–37 (2017).
27. Z. Konôpková, R. S. McWilliams, N. Gómez-Pérez, A. F. Goncharov, Direct measurement of thermal conductivity in solid iron at planetary core conditions. *Nature* **534**, 99–101 (2016).
28. J. C. E. Irving, S. Cottaar, V. Lekić, Seismically determined elastic parameters for Earth's outer core. *Sci. Adv.* **4**, eaar2538 (2018).
29. T. Lay, J. Hernlund, B. A. Buffett, Core–mantle boundary heat flow. *Nat. Geosci.* **1**, 25 (2008).
30. H. Gomi et al., The high conductivity of iron and thermal evolution of the earth's core. *Phys. Earth Planet. Inter.* **224**, 88–103 (2013).
31. M. D. Hammer, G. A. Cox, W. J. Brown, C. D. Beggan, C. C. Finlay, Geomagnetic Virtual Observatories: Monitoring geomagnetic secular variation with the Swarm satellites. *Earth Planets Space* **73**, 54 (2021).
32. L. Huder, N. Gillet, F. Thollard, pygeodyn 1.1. 0: A Python package for geomagnetic data assimilation. *Geosci. Model Dev.* **12**, 3795–3803 (2019).
33. N. Gillet, N. Schaeffer, D. Jault, Rationale and geophysical evidence for quasi-geostrophic rapid dynamics within the Earth's outer core. *Phys. Earth Planet. Inter.* **187**, 380–390 (2011).
34. S. Maffei, A. Jackson, P. W. Livermore, Characterization of columnar inertial modes in rapidly rotating spheres and spheroids. *Proc. Math. Phys. Eng. Sci.* **473**, 20170181 (2017).
35. P. H. Roberts, J. M. Aurnou, On the theory of core-mantle coupling. *Geophys. Astrophys. Fluid Dyn.* **106**, 157–230 (2012).
36. M. Pozzo, C. Davies, D. Gubbins, D. Alfè, Thermal and electrical conductivity of iron at Earth's core conditions. *Nature* **485**, 355–358 (2012).
37. N. Schaeffer, D. Jault, H. C. Nataf, A. Fournier, Turbulent geodynamo simulations: A leap towards Earth's core. *Geophys. J. Int.* **211**, 1–29 (2017).
38. D. Jault, C. C. Finlay, "Waves in the core and mechanical core-mantle interactions" in *Core Dynamics*, G. Schubert, P. Olson, Eds. (Treatise on Geophysics, Elsevier, Oxford, ed. 2, 2015), vol. 8, pp. 225–244.
39. F. Gerick et al., Data and code used in "Satellite magnetic data reveal interannual waves in Earth's core." Zenodo. https://doi.org/10.5281/zenodo.5084367. Deposited 28 February 2022.